**Atmospheric
Measurement
Techniques**

Ground-based FTIR water vapour profile analyses

M. Schneider and F. Hase

IMK-ASF, Forschungszentrum Karlsruhe und Universität Karlsruhe, Karlsruhe, Germany

Abstract. Due to a large vertical gradient and strong variability of water vapour, algorithms that are effectively applied for ground-based remote sensing of many different atmospheric trace gases can be insufficient for the retrieval of tropospheric water vapour profiles. We review the most important features of the retrieval and of the radiative transfer modelling required for accurate monitoring of tropospheric water vapour profiles by ground-based FTIR (Fourier Transform Infrared) experiments. These are: a fit of a variety of different water vapour lines with different strength, a logarithmic scale inversion, a speed dependent Voigt line shape model, and a joint temperature profile retrieval. Furthermore, the introduction of an interspecies constraint allows for a monitoring of HDO/H_2O ratio profiles.

1 Introduction

Water vapour is the most important greenhouse gas and thus, continuous observations of tropospheric water vapour amounts are essential for climate change research. The radiative forcing of water vapour depends strongly on the altitude. In the middle and upper troposphere, it is much more effective as a greenhouse gas than in the lower troposphere (e.g. Spencer and Braswell, 1997; Held and Soden, 2000). Consequently, the long-term observations of middle/upper tropospheric water vapour amounts are of particular interest. Traditionally, operational radiosondes measure upper-air water vapour. Although there are large efforts for reducing the uncertainties of the radiosonde data (e.g. Leiterer et al., 2005; Miloshevich et al., 2009), the consistency of the radiosonde data set remains questionable, since a variety of different sensor types has been applied during the last decades. There are

even inconsistencies for sensors of the same type but with different manufacturing dates (Turner et al., 2003). It is difficult to use these data for trend analyses and climate studies.

Ground-based high quality remote sensing experiments have the potential to monitor atmospheric trace gases in a rather consistent manner. In the framework of NDACC (Network for Detection of Atmospheric Composition Change, Kurylo, 2000), high quality solar absorption spectra have been measured over many years and at many different sites with the same type of instrument. These measurements disclose significant information about the distribution of many different atmospheric trace gases. Over the last decades, the NDACC FTIR experiments contributed to the study of stratospheric ozone chemistry by providing a long-term dataset of different ozone relevant trace gases (e.g. Rinsland et al., 2003; Vigouroux et al., 2008). During the last years, the NDACC-FTIR community has increased its efforts of monitoring the tropospheric distribution of greenhouse gases, including water vapour. Since the NDACC FTIR experiments are regularly characterised by low pressure gas cell measurements (Hase et al., 1999), the FTIR data can serve as a more reliable source for water vapour trend studies than the radiosonde data, especially in the upper troposphere. Furthermore, the FTIR raw data (measured solar absorption spectra) are stored and can be reprocessed whenever there is some progress in the analysis method. Analysis methods for atmospheric remote sensing are treated extensively in the textbook of C. D. Rodgers (e.g. Rodgers, 2000). However, the retrieval of atmospheric water vapour amounts from ground-based FTIR spectra is an advanced atmospheric inversion problem. The large vertical gradient and variability is the main reason why a standard retrieval set up is not suitable. First vertical profiles of water vapour measured by ground-based FTIR experiments were reported by a group of the Institute for Meteorology and Climate Research, Karlsruhe, Germany (in German letters: IMK-ASF; Hase et al., 2004). During the last years, the IMK-ASF water vapour analysis

has been continuously developed and improved (Schneider et al., 2006a,b; Schneider and Hase, 2009). These efforts made it possible to monitor tropospheric H_2O profiles (including upper tropospheric amounts) and HDO/H_2O ratio profiles by ground-based FTIR experiments.

This paper reviews the aspects of an effective ground-based FTIR water vapour profile analysis. Section 2 briefly describes the principles of a ground-based FTIR analysis and in Sect. 3 we discuss the methods developed at IMK-ASF to overcome the difficulties of water vapour analysis. Section 4 lists these developments in the order of their importance.

2   General setup of a ground-based FTIR analysis

The basic equation for analysing solar absorption spectra is Lambert Beer's law:

$$I(\lambda) = I_{sun}(\lambda) \exp\left(-\int_{TOA}^{Obs.} \sigma_x(\lambda, s(T, p))x(s)ds\right) \qquad (1)$$

Here $I(\lambda)$ is the measured intensity at wavelength λ, I_{sun} the solar intensity, $\sigma_x(\lambda, s)$ is the absorption cross section and $x(s)$ the concentration of an absorber x at location s. The integration is performed along the path of the direct sunlight (between the Observer (Obs.) and the Top of the atmosphere (TOA)). The spectra are simulated by a precise line-by-line radiative transfer model applying the parameters of spectroscopic databases (e.g. HITRAN, Rothman et al., 2005). Within NDACC mid-infrared ground-based FTIR spectra are typically measured with a resolution of $0.005 \, cm^{-1}$. Equation (1) neglects atmospheric emission. However, at low frequencies (below approximately $1000 \, cm^{-1}$) or when analysing lunar absorption spectra (Palm et al., 2008), it should be considered by adding an atmospheric emission correction term.

For the purpose of numerical handling, the atmospheric state $x(s)$ and the simulated spectrum $I(\lambda)$ are discretised in form of a state vector $\boldsymbol{x}$ and a measurement vector $\boldsymbol{y}$. The measurement and state vector are related by a vector valued function $\boldsymbol{F}$ which simulates the atmospheric radiative transfer and the characteristics of the measurement system (spectral resolution, instrumental line shape, etc.):

$$\boldsymbol{y} = \boldsymbol{F}(\boldsymbol{x}) \qquad (2)$$

The derivatives $\partial y/\partial x$ determine the changes in the spectral fluxes $\boldsymbol{y}$ for changes in the vertical distribution of the absorber $\boldsymbol{x}$. These derivatives are collected in a Jacobian matrix $\mathbf{K}$:

$$\partial \boldsymbol{y} = \mathbf{K}\partial \boldsymbol{x} \qquad (3)$$

Direct inversion of Eq. (3) would allow an iterative calculation of the sought variables $\boldsymbol{x}$. However, the problem is generally under-determined, i.e. the columns of $\mathbf{K}$ are not linearly independent and there are many solutions that are in acceptable agreement with the measurement. An optimal estimation (OE) approach removes this ambiguity. It combines the measurement information with the a priori assumption about the atmospheric state and selects the most probable state for the given measurement. The solution is the maximum value of a conditional probability density function (pdf), which is the product of two pdfs: a first, describing the statistics of the differences between simulated and measured spectra (measurement noise covariance $\mathbf{S}_\epsilon$), and a second, describing the a priori knowledge of the atmospheric state (mean state $\boldsymbol{x_a}$ and covariance $\mathbf{S_a}$). The maximum value of the conditional pdf is reached at the minimum of its negative logarithm. Assuming pure Gaussian statistics, we have to minimise:

$$[\boldsymbol{y} - \boldsymbol{F}(\boldsymbol{x})]^T \mathbf{S}_\epsilon^{-1} [\boldsymbol{y} - \boldsymbol{F}(\boldsymbol{x})]$$
$$+[\boldsymbol{x} - \boldsymbol{x}_a]^T \mathbf{S_a}^{-1} [\boldsymbol{x} - \boldsymbol{x}_a] \qquad (4)$$

Due to the nonlinear behaviour of the Lambert Beer law (Eq. 1), the cost function (Eq. 4) is minimised iteratively by a Gauss-Newton method. The solution for the $(i+1)th$ iteration is (Rodgers, 2000):

$$\boldsymbol{x}_{i+1} = \boldsymbol{x}_a + \mathbf{S_a}\mathbf{K_i}^T (\mathbf{K_i}\mathbf{S_a}\mathbf{K_i}^T + \mathbf{S}_\epsilon)^{-1}$$
$$[\boldsymbol{y} - \boldsymbol{F}(\boldsymbol{x}_i) + \mathbf{K_i}(\boldsymbol{x}_i - \boldsymbol{x}_a)] \qquad (5)$$

An important component of the retrieved solution is the averaging kernel matrix $\mathbf{A}$:

$$\mathbf{A} = (\mathbf{K}^T \mathbf{S}_\epsilon^{-1} \mathbf{K} + \mathbf{S_a}^{-1})^{-1} \mathbf{K}^T \mathbf{S}_\epsilon^{-1} \mathbf{K} \qquad (6)$$

The averaging kernel matrix $\mathbf{A}$ documents the sensitivity and the vertical smoothing of the remote sensing system. It relates the real variability $(\boldsymbol{x} - \boldsymbol{x_a})$ to the measured variability $(\hat{\boldsymbol{x}} - \boldsymbol{x_a})$:

$$(\hat{\boldsymbol{x}} - \boldsymbol{x_a}) = \hat{\mathbf{A}}(\boldsymbol{x} - \boldsymbol{x_a}) \qquad (7)$$

whereby $\hat{\mathbf{A}}$ is the averaging kernel matrix as calculated at the solution state $\hat{\boldsymbol{x}}$. In addition, the trace of $\hat{\mathbf{A}}$ quantifies the amount of information introduced by the measurement. It can be interpreted in terms of degrees of freedom of the measurement (DOF).

3   Particularities of a water vapour analysis

In recent years at IMK-ASF, we continuously extended the standard FTIR analysis by several innovative features, which enables the analysis of water vapour profiles. The features are as follows: first, the application of a variety of weak and strong water vapour lines, which makes the retrievals very sensitive to both extremely low and high water vapour amounts. Second, a logarithmic scale inversion. Only this assures a proper constraint of tropospheric water vapour amounts (Schneider et al., 2006a; Worden et al., 2006a; Deeter et al., 2007). Third, a constraint of H_2O profiles against HDO profiles, which allows for a retrieval of tropospheric HDO/H_2O ratio profiles (Schneider et al., 2006b;

Worden et al., 2006a) and also improves the results for H_2O. The HDO/H_2O ratio profiles are useful for investigating the transport pathways of tropospheric water vapour. Fourth, the application of optimised spectroscopic parameters including a non-Voigt line shape model for a proper simulation of the water vapour lines (Boone et al., 2007; Schneider and Hase, 2009). Fifth, the consideration of atmospheric emissions for a proper simulation of radiances at low frequencies. And sixth, a simultaneous temperature profile inversion. This reduces two important error sources of ground-based FTIR measurements, which are uncertainties in the assumed temperature profiles and uncertainties in the temperature dependence of the applied spectroscopic parameters (Schneider et al., 2006a; Schneider and Hase, 2008; Schneider et al., 2008).

In the following subsections, we document the improvements achieved by these innovations, therefore, we document the performance of 6 different FTIR analysis setups:

– lin: inversion on a linear scale.

– log: inversion on a logarithmic scale.

– log, isc: log-scale and H_2O, $H_2^{18}O$, and HDO interspecies constraint.

– log, isc, nV: log-scale, inter-species constraint, and non-Voigt line shape model.

– log, isc, nV, ae: log-scale, inter-species constraint, non-Voigt line shape, and correction for atmospheric emission.

– log, isc, nV, ae, T: log-scale, inter-species constraint, non-Voigt line shape, atmospheric emission, and simultaneous temperature profile retrieval.

The documentation consists of a theoretical part, by analysing the DOF values achieved by the different analysis setups, and of an empirical part, by comparing the FTIR profiles to radiosonde measurements. We do this, taking measurements performed at the Izaña Atmospheric Research Centre (in Spanish letters: CIAI) as an example, since at CIAI water vapour radiosonde measurements (Vaisala RS92) are performed twice daily. The quality documentation is based on a representative set of measurements, which cover a large variety of different atmospheric water vapour states, taken on 93 different days between June 2005 and February 2007.

Concerning the empirical validation, we have to consider that an FTIR measurement takes less than 10 min, but a radiosonde needs about 1 hour to measure a profile from the ground to 15 km. As temporal coincidence criterion we require that the RS92 radiosonde is located at 7.5 km within 2 h of the FTIR measurement. In addition, it is important to take into account the relatively modest vertical resolution of the ground-based FTIR profiles, which is documented by the averaging kernel matrix $\hat{\mathbf{A}}$. Figure 1 shows the columns of a
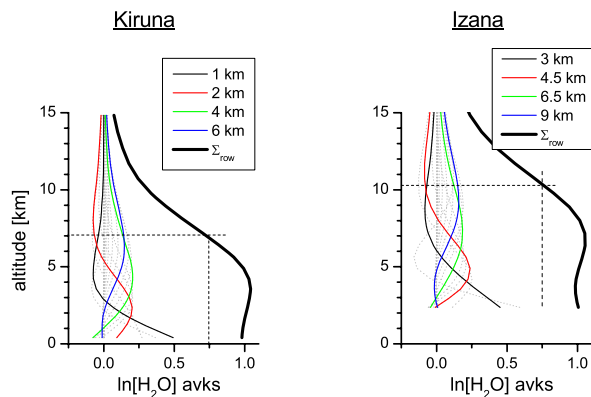

Fig. 1. Typical averaging kernels for ground-based FTIR remote sensing of water vapour. Left panel: for the subarctic site of Kiruna (68° N, 420 m a.s.l.); right panel: for the subtropical site of Izaña (28° N, 2370 m a.s.l.). The kernels for the selected heights as given in the legend are highlighted by solid black, red, green, and blue, respectively. The total sensitivity ($\sum_{row}$) is depicted as a thick black line.

typical averaging kernel matrix $\hat{\mathbf{A}}$ for two very distinct sites: for the subarctic site of Kiruna (Northern Sweden, 67°50′ N, 20°25′ E at 420 m a.s.l.), on the left panel, and for Izaña (Tenerife Island, Spain, 28°18′ N, 16°29′ W at 2370 m a.s.l.), on the right panel. At both sites the FTIR system is very sensitive up to the upper troposphere (sum along the rows of $\hat{\mathbf{A}}$, i.e. $\sum_{row} > 75\%$, see thick black line). The vertical resolution is 2 km in the lower troposphere, 4 km in the middle troposphere and 6 km in the upper troposphere (see solid lines highlighted by different colours). For the comparison, we adjust the vertically highly-resolved Vaisala RS92 profile (x_{RS92}) to the modest vertical resolution of the FTIR profiles by a convolution with the FTIR averaging kernels $\hat{\mathbf{A}}$. According to Eq. (7) it is:

$$\hat{x}_{RS92} = \hat{\mathbf{A}}(x_{RS92} - x_a) + x_a \tag{8}$$

The result is an RS92 profile ($\hat{x}_{RS92}$) with the same vertical resolution and sensitivity as the FTIR profile. In addition, we apply the temperature and radiation correction for the RS92 sensor as suggested by Vömel et al. (2007). We would like to remark that smoothing according to Eq. (8) is an approximation since we deal with a nonlinear problem, whereas Eq. (8) assumes linearity between x_{RS92} and x_a. However, as long as the individual averaging kernels (the averaging kernels $\hat{\mathbf{A}}$ at the solution state) are used, this approximation is still applicable.

3.1 Simultaneous fit of weak and strong lines

Atmospheric water vapour is highly variable, e.g. the total precipitable water vapour (PWV) amount varies almost over 2 orders of magnitude. This requires the application of water
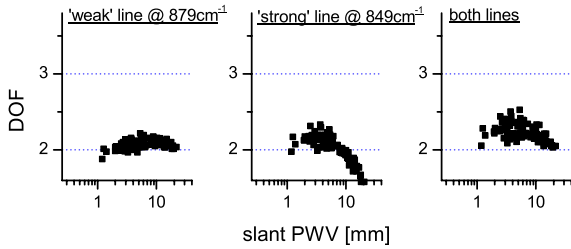
Fig. 2. Dependence of DOF values on slant PWV for the application of different water vapour signatures. Left panel: weak line at 879 cm^{-1}; Middle panel: strong line at 849 cm^{-1}; Right panel: Both weak and strong line at 879 cm^{-1} and 849 cm^{-1}.

vapour lines with different characteristics. Strong lines are necessary to be sensitive in the case of low water vapour amounts. However, these lines are saturated at large water vapour amounts. Therefore, weak lines have to be included into the spectral microwindows. Figure 2 shows the degrees of freedom of the measurement (DOF) versus the total water vapour content along the line of sight (slant PWV). If we apply a spectral microwindow with a weak water vapour line, the DOF value is around 2.1, but tends to lower values for slant PWVs below 3 mm (left panel). The central panel shows the situation when applying a strong line. For slant PWVs below 8 mm we obtain larger DOF values if compared to the "weak line retrieval". However, this strong line is saturated for slant PWVs above 10 mm. For large slant PWVs the DOF values are rapidly decreasing. The right panel depicts the DOFs for a retrieval which applies both the weak and the strong line. Then we achieve similar results in the case of low and high slant PWVs.

Our IMK-ASF water vapour analysis algorithm applies 49 water vapour lines of different strength (37 H$_2$O, 3 H$_2^{18}$O, and 9 HDO lines) between 790 and 1330 cm^{-1}. The corresponding spectral microwindows are shown in Fig. 3. With this setup we achieve DOF values between 2.2 and 3.0 (see Fig. 4).

3.2 Logarithmic scale inversion

Equation (4) assumes Gaussian statistics for the measurement noise and the a priori covariance. While Gaussian statistics is a valid assumption for the measurement noise, it is not necessarily valid for the distribution of the absorber. Highly variable absorbers like water vapour do not follow a Gaussian statistic. However, by performing the inversion on a linear scale, we implicitly assume a normal distribution. Under these circumstances minimising the cost function (Eq. 4) does not yield a statistically optimal solution. If the inversion is performed on a linear scale, the FTIR profiles significantly disagree with the RS92 profiles which is documented by the left panels of Fig. 5: the top panel depicts the differences of all 93 FTIR/RS92 coincidences and

the bottom panel its statistics (mean and standard deviation of the difference). Frequently, the FTIR analysis produces physically impossible negative volume mixing ratios, i.e. $\frac{\text{FTIR}}{\text{RS92}} - 1 < -100\%$.

Like most highly variable atmospheric constituents, water vapour is quite well log-normally distributed and so we can improve the optimal estimation formalism of Eqs. (4) and (5) by transforming the absorber's amounts to a logarithmic scale: if x is log-normally distributed $\ln(x)$ is normally distributed and Eqs. (4) and (5) remain valid. The second panels from the left show the comparison of the RS92 and FTIR profiles when the inversion is performed on a logarithmic scale. The log-scale inversion significantly reduces the scatter between the RS92 and the FTIR data, particularly below 7 km. At higher altitudes the scatter is increased, which is due to the increased sensitivity of the log-scale inversion, whereas for the linear scale inversion both the smoothed sonde profile and the FTIR profile stick to the a priori value. Figure 4 depicts the degrees of freedom of the measurement (DOF) versus the PWV (PWV is calculated by integration of the vertical profiles over altitude). The left panel shows the situation for a linear scale inversion and the second panel from the left for a logarithmic scale inversion. These plots give further insight into the deficiencies of a linear scale water vapour inversion. We observe that for a linear scale inversion the DOF decreases continuously with increasing PWV. This strong dependence is due to an inadequate constraint caused by applying a wrong a priori statistics. At low PWVs the constraint is too weak and at large PWVs it is too strong. The DOF values, in case of a logarithmic scale inversion, show a much weaker dependence on PWV. Its DOF values only decrease when an increasing number of lines become saturated (for slant PWVs above 7 mm).

For an evaluation of the PWVs determined by the different FTIR analyses, we use the coincident PWV measurements of the RS92 and Izaña's Cimel sunphotometer (Holben et al., 1998). We only compare if all three experiments are performed within 1 hour (88 coincidences). For these coincidences the scatter of $\frac{(\text{RS92} - \text{Cimel})}{(\text{RS92} + \text{Cimel})/2}$ is 19.6%. For a linear scale inversion the scatter of $\frac{(\text{FTIR} - \text{RS92})}{(\text{FTIR} + \text{RS92})/2}$ and $\frac{(\text{FTIR} - \text{Cimel})}{(\text{FTIR} + \text{Cimel})/2}$ are 14.5% and 13.5%, respectively. The root-square-sum (RSS) of these values is $\sqrt{14.5^2 + 13.5^2}\% = 19.8\%$. Assuming that all three experiments observe the same airmasses and that their errors (ϵ) are independent, this RSS value is the error sum of Cimel, RS92, and 2×FTIR:

$$
\text{RSS} = \sqrt{\left(\frac{(\text{FTIR} - \text{RS92})}{(\text{FTIR} + \text{RS92})/2}\right)^2 + \left(\frac{(\text{FTIR} - \text{Cimel})}{(\text{FTIR} + \text{Cimel})/2}\right)^2}
$$
$$
= \sqrt{\epsilon_{\text{Cimel}}^2 + \epsilon_{\text{RS92}}^2 + 2\epsilon_{\text{FTIR}}^2} \tag{9}
$$

The precision of the FTIR PWV data can then be estimated to $\sqrt{\frac{19.8^2 - 19.6^2}{2}}\% = 2.0\%$. Table 1 collects the scatter between
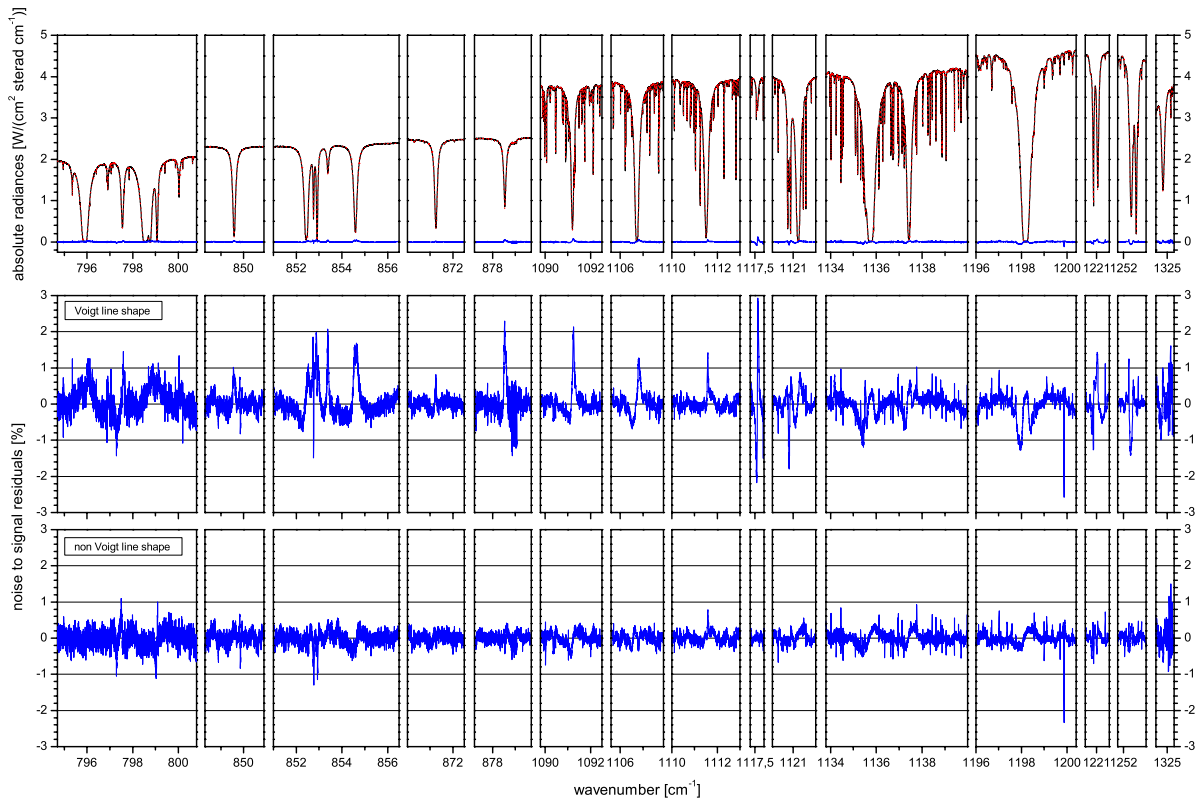
Fig. 3. The 15 spectral windows used for the retrieval of water vapour profiles for typical atmospheric conditions at CIAI (slant PWV of 6.1 mm). The spectral resolution of a typical measurement is $0.005\,\mathrm{cm}^{-1}$. Top panels: black line: measurement; dotted red line: simulation; blue line: residuals relative to maximum radiances, i.e. (measurement−simulation)/max(measurement). Central panels: Zoomed out residuals when applying a Voigt line shape model and the HITRAN 2004 parameters (Rothman et al., 2005) with the water vapour update of Gordon et al. (2007) (depicted as noise to signal ratio); Bottom panels: same as central panel but for a speed dependent Voigt line shape model and the parameters of Schneider and Hase (2009).
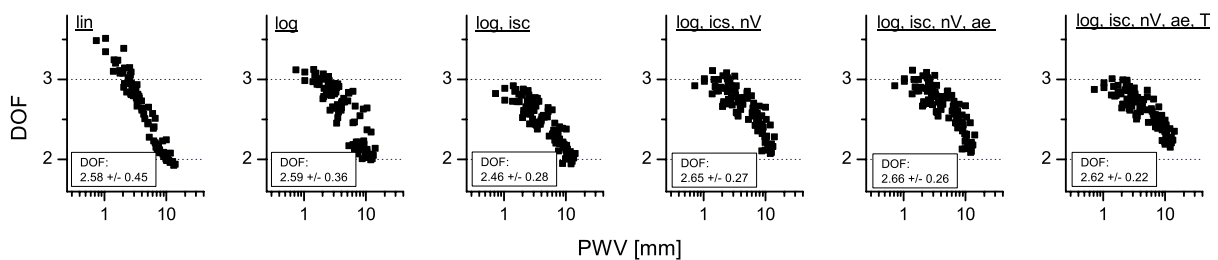

Fig. 4. Dependence of DOF values on PWV for the same different inversion approaches as in Fig. 5. The mean DOF value as well as its 1σ variability are noted in each panel.

the PWVs determined by the different FTIR analyses and by RS92 and Cimel sunphotometer (Holben et al., 1998) measurements. For all the different retrieval setups the error sum of Cimel, RS92, and FTIR, approximated by the RSS value, is very similar to the error sum of Cimel and RS92 of 19.6%. This suggests that the FTIR PWV data are very precise and

that the different retrieval setups – although strongly affecting the profile shape – do not significantly change the retrieved PWV values.

Often the RSS (RS92+Cimel+FTIR error sum) is smaller than the RS92+Cimel error sum of 19.6%. We think that this is caused by the observation of different airmasses by
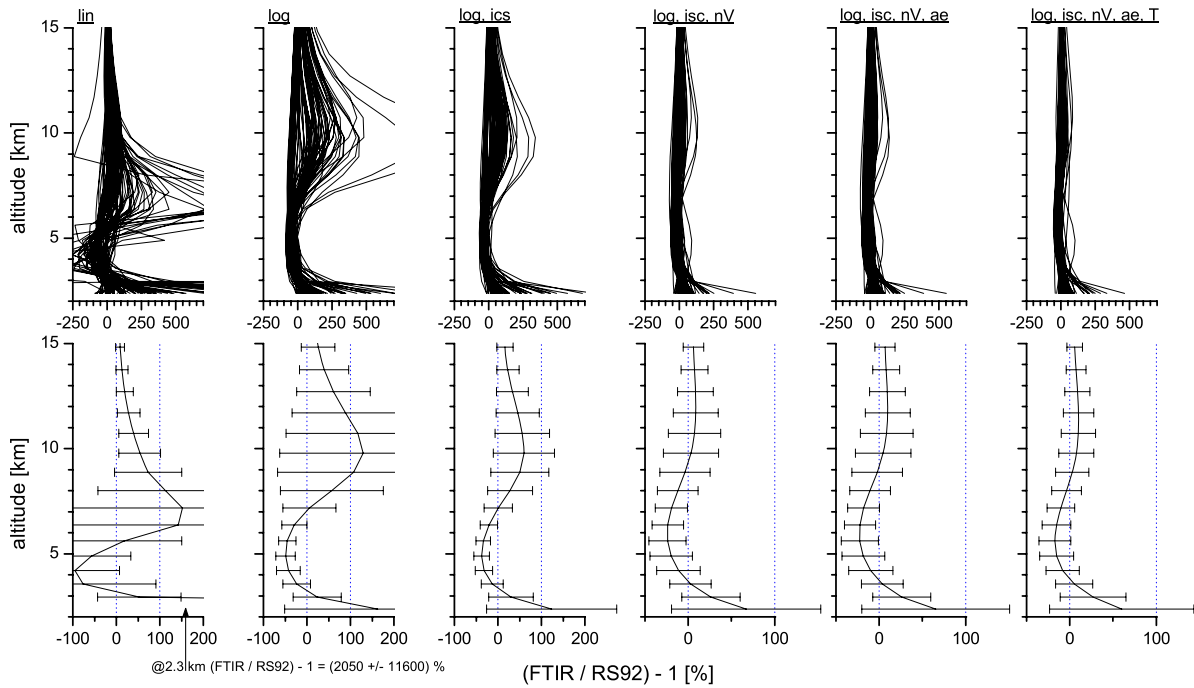
Fig. 5. Difference between smoothed Vaisala RS92 profiles and FTIR profiles for different inversion approaches. Top panels: Individual differences for 93 coincidences (between June 2005 and February 2007); Bottom panels: statistics of the differences (mean and standard deviation). From the left to the right: lin: inversion on a linear scale; log: inversion on a logarithmic scale; log, isc: log-scale inversion and application of an HDO/H_2O inter-species constraint; log, isc, nV: log-scale, inter-species constraint, and application of a speed dependent Voigt line shape model; log, isc, nV, ae: log-scale, inter-species constraint, speed dependent Voigt line shape, and consideration of atmospheric emission; log, isc, nV, ae, T: log-scale, inter-species constraint, speed dependent Voigt line shape, atmospheric emission, and simultaneous temperature profile inversion. Please note that for the three rightmost bottom panels the x-axis scale is amplified by a factor 2.

Table 1. Scatter between PWVs of FTIR, RS92 and Cimel sunphotometer for the different FTIR retrieval setups. First column: scatter of FTIR−RS92; Second column: scatter of FTIR−Cimel sunphotometer; Third column: root-square-sum of scatter FTIR−RS92 and FTIR−Cimel. The Cimel data are courtesy of P. Goloub, University of Lille, France (PI of Izaña's Cimel experiment).

	FTIR −RS92	FTIR −Cimel	RSS
lin	±14.5%	±13.5%	±19.8%
log	±14.1%	±13.4%	±19.5%
log, isc	±13.8%	±13.3%	±19.2%
log, isc, nV	±14.2%	±13.4%	±19.6%
log, isc, nV, ae	±14.2%	±13.3%	±19.5%
log, isc, nV, ae, T	±14.1%	±13.1%	±19.2%

the different experiments. Different airmasses are observed since it is impossible to guarantee that the measurements coincide perfectly, neither in time nor in space. While the RS92 measures the airmass in-situ at the location of the ra-

diosonde, the Cimel and the FTIR detect the water vapour amounts between the instrument and the Sun. Concerning temporal coincidence, the situation is straight forward in the case of Cimel and FTIR since both measurements are performed within several minutes. But for the RS92 the situation is more complex, since the sonde takes more than one hour to travel throughout the troposphere.

3.3 HDO/H$_2$O ratio profiles

The isotopic composition of tropospheric water vapour depends on the ocean surface conditions where it evaporates and on its atmospheric transport pathways. Measurements of HDO/H_2O are a powerful tool for investigating atmospheric dynamics and, in particular, water vapour transport pathways (Worden et al., 2006b; Yoshimura et al., 2008; Frankenberg et al., 2009), which in turn is important for a better understanding of global climate change (water vapour feedback effect). Infrared remote sensing offers a unique opportunity for a continuous observation of the HDO/H$_2$O ratio, which is typically expressed in the form of a δD value. The δD value is the relative difference of the actual HDO/H$_2$O ratio to the standard HDO/H$_2$O ratio called SMOW (Standard Mean

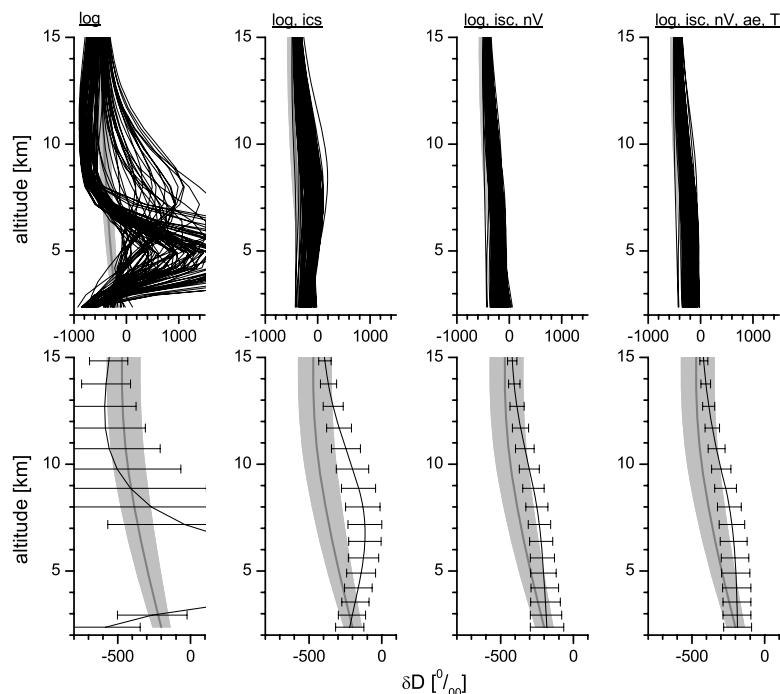**Fig. 6.** δD profiles produced by different inversion approaches. Top panels: Individual profiles for the ensemble of the FTIR/RS92 coincidences; Bottom panels: statistics of the δD profiles (mean and standard deviation represented by black line and error bars, respectively). The grey line and shaded area depicts the mean and standard deviation as calculated from several in-situ measurements (Ehhalt, 1974; Zahn, 2001). From the left to the right: log: log-scale inversion; log, isc: log-scale inversion and application of an HDO/H$_2$O inter-species constraint; log, isc, nV: log-scale, inter-species constraint, and application of a speed dependent Voigt line shape model; log, isc, nV, ae, T: log-scale, inter-species constraint, speed dependent Voigt line shape, atmospheric emission, and simultaneous temperature profile inversion.

Ocean Water) in permil (δD$=1000\times(\frac{[HDO]/[H2O]}{SMOW}-1)$).

Figure 6 shows δD profiles as obtained from different analysis algorithms. The left panel shows the situation for independent H$_2$O and HDO inversions. Then the δD values vary between -1000 and $+4000$, which is physically impossible. The reason for these large errors is the absence of an HDO/H$_2$O constraint. Since H$_2$O and HDO profiles have different vertical resolutions their profiles are not comparable and by using a simple ratio produces unreasonable results. The logarithmic scale inversion allows for an optimal estimation of HDO/H$_2$O profiles, by constraining ln[HDO]$-$ln[H$_2$O] (Schneider et al., 2006b; Worden et al., 2006a). This procedure produces statistically optimised HDO/H$_2$O profiles, which are depicted in the second panel from the left of Fig. 6. Applying the HDO versus H$_2$O inter-species constraints, we observe reasonable HDO/H$_2$O ratios between -700 and $+50$.

The inter-species constraint also improves the agreement between RS92 and FTIR water vapour profiles, as can be seen in the third panel from the left of Fig. 5. Atmospheric HDO amounts are by more than three orders of magnitude lower than H$_2$O amounts. Whereas if we have to fit H$_2$O lines corresponding to transitions between states with high

quantum numbers, we can fit HDO lines which involve states with low quantum numbers. The spectroscopic line parameters, used for describing the absorption signatures, are obtained from laboratory measurements interpreted in terms of quantum theoretical calculations. The measurements, as well as the calculations, are less reliable for transitions involving high quantum number states. These lines are very weak which makes accurate laboratory measurements difficult and corresponding quantum theoretical calculations less constrained by experimental data. It is therefore reasonable to assume that the spectroscopic knowledge of the strongest HDO lines is better than the spectroscopic knowledge of the weak H$_2$O transitions. The inter-species constraint partly reduces the misinterpretation of the H$_2$O signatures, but, due to inconsistencies between the H$_2$O and the HDO line parameters, it increases the residuals (difference between measured and simulated spectrum). As a consequence, the DOF values are slightly reduced (see third panel from the left of Fig. 4).

3.4 Improvement of spectroscopic description

Applying lines with different strength and pressure broadening coefficients theoretically increases the DOF value, but in practice there is no realistic water vapour profile that brings measured and simulated signatures of all the different lines to a reasonable agreement. In Schneider and Hase (2009), we analysed this problem in more detail and found that optimising the spectroscopic parameters, including a speed dependent Voigt line shape model instead of a Voigt line shape model, provides a much better agreement between the simulated and measured high-resolution spectra and at the same time improves the quality of the retrieved water vapour profiles. This coincides with Boone et al. (2007) who recommended the application of a speed dependent Voigt line shape model when analysing the infrared spectra measured by ACE (Atmospheric Chemistry Experiment). The improved agreement between measured and simulated spectrum becomes obvious when the two panels from the bottom of Fig. 3 are compared. The first panel shows the residuals (difference between measured and simulated spectrum) when applying a Voigt line shape model and the HITRAN 2004 parameters (Rothman et al., 2005) with the water vapour update of Gordon et al. (2007). The second panel depicts the residuals for a speed dependent Voigt line shape model that applies the parameters of Schneider and Hase (2009). The improvement in the quality of the retrieved water vapour profile is documented in Fig. 5 when comparing the third panel from the left, where profiles are retrieved by applying a Voigt line shape model and the Gordon et al. (2007) water vapour line parameters, with the fourth panel from the left, where a speed dependent Voigt line shape model and the Schneider and Hase (2009) parameters are applied.

In addition, applying a refined line shape model allows for a further improved interpretation of the measured spectrum and leads to larger DOF values. This can be observed by comparing the third and the fourth panel from the left of Fig. 4.

Figure 6 demonstrates that applying a speed dependent Voigt line shape model also improves the quality of the δD profiles. They are now in reasonable agreement with the a priori expected δD profiles (third panel from the left), whereas the δD profiles produced by applying a Voigt line shape model show an unexpected maximum at about 7 km (second panel from the left).

3.5 Atmospheric emissions

Some line-by-line models used for simulating solar absorption spectra approximate the radiances by applying Eq. (1) disregarding atmospheric self emission. Figure 7 shows the relative absorption at the line centres (i.e. baseline offset at the line centre related to the radiances at the line shoulders) of two strong water vapour lines versus the slant PWVs. The black squares show the measurement. Both lines are satu-
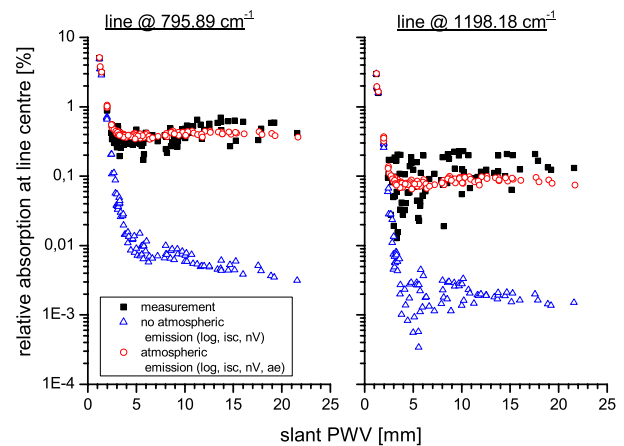

Fig. 7. Relative baseline offset $\left(\frac{\text{radiances at line centre}}{\text{radiances at line shoulder}} \right)$ at the centres of strong water vapour lines. Left panel: line at low frequency (795 cm^{-1}); Right panel: line at higher frequency (1198 cm^{-1}). Black squares: measurement; Blue triangle: no consideration of atmospheric emission; Red circles: consideration of atmospheric emission.

rated for slant PWVs above 3 mm. We observe that the baseline offset at 796 cm^{-1} is 0.4%, and at 1198 cm^{-1} it is 0.1%. We find that for frequencies below approx. 1000 cm^{-1} the baseline offset caused by atmospheric emission is larger than the measurement noise. The blue triangles depict radiances simulated according to Eq. (1), i.e. by disregarding atmospheric emission, and the red circles show the calculation which include atmospheric emissions. We observe that the baseline offset is dominated by atmospheric emission.

The consideration of atmospheric emission prevents a misinterpretation of the strong water vapour signatures at low frequencies. Considering the atmospheric emission slightly increases the DOF values by 0.1 and reduces the DOF 1σ variability by 0.1 (compare forth and fifth panel from the left of Fig. 4). In addition, it slightly improves the quality of the FTIR water vapour profiles (the scatter and mean difference to the RS92 profile are reduced; compare fourth and fifth panel from the left of Fig. 5). In the case of solar absorption spectra, these effects are very small since the intensity of the atmospheric emission is less than 0.5% of the solar intensity. However, when analysing lunar absorption spectra, it is essential to consider atmospheric emission (Palm et al., 2008).

3.6 Joint retrieval of temperature profiles

The cross sections σ_x (see Eq. 1) depend on temperature and pressure. Standard inversion algorithms apply temperature profiles from meteorological reanalyses or data measured close to the FTIR site by radiosondes. However, these data may be erroneous, first, due to errors in the radiosonde observations (reanalysis data are also based on radiosonde

measurements), and second, due to temporal and spatial mismatch between radiosonde and FTIR measurements. Schneider and Hase (2008) showed that for standard O_3 inversions these temperature uncertainties are the leading error source and they suggested to retrieve the temperature profile simultaneously with the trace gas profile. In the case of O_3, a joint retrieval of temperature profiles significantly improves the quality of the FTIR O_3 data (Schneider and Hase, 2008; Schneider et al., 2008).

The fifth and sixth panel from the left of Fig. 5 document how a joint retrieval of temperature profiles improves the quality of the FTIR water vapour profiles. If the reanalysis or radiosonde temperatures are used, we observe a mean difference and scatter between RS92 and FTIR of $(+26.1\pm33.5)\%$ at 3 km, $(-18.3\pm24.8)\%$ at 5 km, and $(-2.3\pm29.4)\%$ at 9 km. For a joint inversion of the temperature profile, we get $(-15.3\pm19.7)\%$ and $(+2.7\pm19.3)\%$ at 5 and 9 km, respectively. Then the middle and upper tropospheric FTIR water vapour amounts are of very good quality, since the remaining scatter of about 20% is in agreement with the expected uncertainty of the RS92 data (Vömel et al., 2007). Surprisingly, in the lower troposphere the scatter slightly increases from $\pm33.5\%$ to $\pm38.1\%$. We think that this increase is spurious given the relatively large inhomogeneity in lower tropospheric water vapour fields and the fact that the RS92 and FTIR detect different airmasses.

The joint temperature inversion also reduces the variability in δD values as retrieved for the lower troposphere, from 110 permil to 95 (compare third and fourth panel from the left of Fig. 6), providing for a better agreement with other lower tropospheric δD measurements (e.g. Ehhalt, 1974).

Concerning the DOF values, the joint temperature inversion slightly increases the DOFs for measurements made at high slant PWVs and slightly decreases the DOFs for measurements made at low slant PWVs (see Fig. 4). The 1σ variability of the DOFs for the analysed ensemble reduces to 0.22, i.e. the H_2O results under different atmospheric conditions are more consistent.

4 Conclusions

Tropospheric water vapour is highly variable. For a precise monitoring of both very humid and very dry atmospheric states, the application of many different lines with different strength and pressure broadening coefficients is essential. Furthermore, the inversion must be performed on a logarithmic scale. Only this assures a proper constraint of tropospheric water vapour amounts and a statistically optimal solution. In addition, the logarithmic scale inversion allows for an optimal estimation of HDO/H_2O ratio profiles. A linear scale inversion provides no statistically optimal solution and no possibility for an optimal estimation of HDO/H_2O ratios.

The logarithmic scale inversion is important, but for an effective ground-based FTIR water vapour inversion we need

to remove the inconsistencies when simulating the spectral signatures of a large number of different lines. The inconsistency between the HDO lines (situated above $1220\,\mathrm{cm}^{-1}$) and the H_2O lines (between 775 and $1200\,\mathrm{cm}^{-1}$) is particularly large. The application of a speed dependent Voigt line shape model together with the improved spectroscopic parameters given in Schneider and Hase (2009) removes a large part of these inconsistencies and significantly improves the quality of the FTIR profiles. Applying a large set of weak and strong water vapour signatures, performing the inversion on a log-scale, and using improved spectroscopic parameters including a speed dependent Voigt line shape model adequately exploits ground-based FTIR measurements. The FTIR system then provides tropospheric water vapour profiles precisely better than 25–30% and systematic errors of smaller than 50% as well as reasonable HDO/H_2O ratio profiles. Our analysis recipes significantly reduce the dependency of the DOFs on the atmospheric condition, i.e. they produce consistent profiles even for largely varying atmospheric water vapour contents. Our recipes are essential for retrieving profiles but do not significantly affect the total precipitable water vapour (PWV) amounts. All the different retrieval setups allow a very precise PWV monitoring (precision of about 2%).

Considering atmospheric emission and, in particular, performing a joint temperature profile inversion further improves the quality of the FTIR profiles. Then the systematic difference and scatter between the RS92 and the FTIR data is reduced to 15 and 20%, respectively. This scatter value is close to the expected precision of the RS92 data of 5–20% (Vömel et al., 2007) and this means that when applying all the features of the IMK-ASF water vapour analysis as presented in Sect. 3, a ground-based FTIR system provides tropospheric water vapour profiles with good precision and with the vertical resolution as documented in Fig. 1.

References

Boone, C. D., Walker, K. A., and Bernath, P. F.: Speed-dependent Voigt profile for water vapor in infrared remote sensing applications, J. Quant. Spectrosc. Radiat. Transfer, 105, 525–532, 2007.

Deeter, M. N., Edwards, D. P., and Gille, J. C.: Retrievals of carbon monoxide profiles from MOPITT observations using

lognormal a priori statistics, J. Geophys. Res., 112, D11311, doi:10.1029/2006JD007999, 2007.

Ehhalt, D. H.: Vertical profiles of HTO, HDO, and H_2O in the Troposphere, Rep. NCAR-TN/STR-100, Natl. Cent. for Atmos. Res., Boulder, Colo., 1974.

Frankenberg, C., Yoshimura, K., Warneke, T., Aben, I., Butz, A., Deutscher, N., Griffith, D., Hase F., Notholt, J., Schneider, M., Schrejver, H., and Röckmann, T.: Dynamic processes governing lower-tropospheric HDO/H_2O ratios as observed from space and ground, Science, 325, 1374–1377, doi:10.1126/science.1173791, 2009.

Gordon, E. I., Rothman, L. S., Gamache, R. R., Jacquemart, D., Boone, C., Bernath, P. F., Shephard, M. W., Delamere, J. S., and Clough, S. A.: Current updates of the water-vapor line list in HITRAN: A new "Diet" for air-broadened half-widths, J. Quant. Spectrosc. Radiat. Transfer, 108, 389–402, 2007.

Hase, F., Blumenstock, T., and Paton-Walsh, C.: Analysis of the instrumental line shape of high-resolution Fourier transform IR spectrometers with gas cell measurements and new retrieval software, Appl. Opt., 38, 3417–3422, 1999.

Hase, F., Hannigan, J. W., Coffey, M. T., Goldman, A., Höpfner, M., Jones, N. B., Rinsland, C. P., and Wood, S. W.: Intercomparison of retrieval codes used for the analysis of high-resolution, ground-based FTIR measurements, J. Quant. Spectrosc. Ra., 87, 25–52, 2004.

Held, I. M. and B. J. Soden: Water Vapour Feedback and Global Warming, Annu. Rev. Energy Environ., 25, 441–475, 2000.

Holben, B. N., T. F. Eck, I. Slutsker, D. Tanré, J. P. Buis, Setzer, A., Vermote, E., Reagan, J. A., Kaufman, Y. J., Nakajima, T., F. Lavenu, Jankowiak, I., and Smirnov, A.: AERONET – A Federated Instrument Network and Data Archive for Aerosol Characterization, Remote Sens. Environ., 66, 1–16, 1998.

Kurylo, M. J. and Zander, R.: The NDSC – Its status after 10 years of operation, Proceedings of XIX Quadrennial Ozone Symposium, Hokkaido University, Sapporo, Japan, 167–168, 2000.

Leiterer, U., Deir, H., Nagel, D., Naebert, T., Althausen, D., Franke, K., Kats, A., and Wagner, F.: Correction method for RS80-A Humicap humidity profiles and their validation by Lidar backscattering profiles in tropical cirus clouds, J. Atmos. Oceanic Technol., 22, 18–29, 2005.

Miloshevich, L. M., Vömel, H., Whiteman, D. W., and Leblanc, T.: Accuracy assessment and correction of Vaisala RS92 radiosonde water vapor measurements, J. Geophys. Res., 114, D11305, doi:10.1029/2008JD011565, 2009.

Palm, M., Melsheimer, C., Noël, S., Notholt, J., Burrows, J., and Schrems, O.: Integrated water vapor above Ny Ålesund, Spitsbergen: a multisensor intercomparison, Atmos. Chem. Phys. Discuss., 8, 21171–21199, 2008, http://www.atmos-chem-phys-discuss.net/8/21171/2008/.

Rinsland, C. P., E. Mahieu, R. Zander, Jones, N. B., Chipperfield, M. P., Goldman, A., Anderson, J., Russell III, J. M., Demoulin, P., Notholt, J., Toon, G. C., Blavier, J.-F., Sen, B., Sussmann, R., Wood, S. W., Meier, A., Griffith, D. W. T., Chiou, L. S., Murcray, F. J., Stephen, T. M., Hase, F., Mikuteit, S., Schultz, A., Blumenstock, T.: Long-Term Trends of Inorganic Chlorine from Ground-Based Infrared Solar Spectra: Past Increases and Evidence for Stabilization, J. Geophys. Res., 108(D8), 4252, doi:10.1029/2002JD003001, 2003.

Rodgers, C. D.: Inverse Methods for Atmospheric Sounding: The-

ory and Praxis, World Scientific Publishing Co., Singapore, ISBN 981-02-2740-X, 2000.

Rothman, L. S., Jacquemart, D., Barbe, A., Benner, D. C., Birk, M., Brown, L. R., Carleer, M. R., Chackerian Jr. C., Chance, K. V., Coudert, L. H., Dana, V., Devi, J., Flaud, J.-M., Gamache, R. R., Goldman, A., Hartmann, J. M., Jucks, K. W., Maki, A. G., Mandin, J. Y., Massie, S. T., Orphal, J., Perrin, A., Rinsland, C. P., Smith, M. A. H., Tennyson, J., Tolchenov, R. N., Toth, R. A., Vander-Auwera, J., Varanasi, P., and Wagner, G. The HITRAN 2004 molecular spectroscopic database, J. Quant. Spectrosc. Radiat. Transfer, 96, 139–204, 2005.

Schneider, M., Hase, F., and Blumenstock, T.: Water vapour profiles by ground-based FTIR spectroscopy: study for an optimised retrieval and its validation, Atmos. Chem. Phys., 6, 811–830, 2006a, http://www.atmos-chem-phys.net/6/811/2006/.

Schneider, M., Hase, F., and Blumenstock, T.: Ground-based remote sensing of HDO/H2O ratio profiles: introduction and validation of an innovative retrieval approach, Atmos. Chem. Phys., 6, 4705–4722, 2006b, http://www.atmos-chem-phys.net/6/4705/2006/.

Schneider, M. and Hase, F.: Technical note: Recipe for monitoring of total ozone with a precision of 1 DU applying mid-infrared solar absorption spectra, Atmos. Chem. Phys., 8, 63–71, 2008, http://www.atmos-chem-phys.net/8/63/2008/.

Schneider, M., Redondas, A., Hase, F., Guirado, C., Blumenstock, T., and Cuevas, E.: Comparison of ground-based Brewer and FTIR total column O_3 monitoring techniques, Atmos. Chem. Phys., 8, 5535–5550, 2008, http://www.atmos-chem-phys.net/8/5535/2008/.

Schneider, M. and F. Hase: Improving spectroscopic line parameters by means of atmospheric spectra: Theory and example for water vapour and solar absorption spectra, J. Quant. Spectrosc. Radiat. Transfer, 110, 1825–1839, doi:10.1016/j.jqsrt.2009.04.011, 2009.

Spencer, R. W. and W. D. Braswell: How Dry is the Tropical Free Troposphere? Implications for Global Warming Theory, B. Am. Meteorol. Soc., 78, 1097–1106, 1997.

Turner, D. D., B. M. Lesht, S. A. Clough, J. C. Liljegren, H. E. Revercomb, and D. C. Tobin: Dry bias ans variability in Vaisala RS80-H radiosondes: the ARM experience, J. Atmos. Oceanic Technol., 20, 117–123, 2003.

Vigouroux, C., De Mazière, M., Demoulin, P., Servais, C., Hase, F., Blumenstock, T., Kramer, I., Schneider, M., Mellqvist, J., Strandberg, A., Velazco, V., Notholt, J., Sussmann, R., Stremme, W., Rockmann, A., Gardiner, T., Coleman, M., and Woods, P.: Evaluation of tropospheric and stratospheric ozone trends over Western Europe from ground-based FTIR network observations, Atmos. Chem. Phys., 8, 6865–6886, 2008, http://www.atmos-chem-phys.net/8/6865/2008/.

Vömel, H., Selkirk, H., Miloshevich, L., Valverde, J., Valdés, J., Kyrö, E., Kivi, R., Stolz, W., Peng, G., and Diaz, J. A.: Radiation dry bias of the Vaisala RS92 humidity sensor, J. Atmos. Oceanic Technol., 24, 953–963, 2007.

Worden, J. R., K. Bowman, D. Noone, R. Beer, S. Clough, A. Eldering, B. Fisher, A. Goldman, M. Gunson, R. Herman, S. S. Kulawik, M. Lampel, M. Luo, G. Osterman, C. Rinsland, C. Rodgers, S. Sander, M. Shephard, and H. Worden: TES observations of the tropospheric HDO/H2O ratio: retrieval

approach and characterization, J. Geophys. Res., 111(D16), D16309, doi:10.1029/2005JD006606, 2006a.

Worden, J. R., Noone, D., Bowman, K., Beer, R., Eldering, A., Fisher, B., Gunson,M., Goldman, A., Herman, R., Kulawik, S. S., Lampel, M., Osterman, G., Rinsland, C., Rodgers, C., Sander, S., Shephard, M., Webster, C. R., and Worden, H.: Importance of rain evaporation and continental convection in the tropical water cycle, Nature, 445, 528–532, doi:10.1038/nature05508, 2006b.

Yoshimura, K., Kanamitsu, M., Noone, D., and Oki, T.: Historical isotope simulation using Reanalysis atmospheric data, J. Geophys. Res., 113, D19108, doi:10.1029/2008JD010074, 2008.

Zahn, A.: Constraints on 2-Way Transport across the Arctic Tropopause Based on O_3, Stratospheric Tracer (SF_6) Ages, and Water Vapor Isotope (D, T) Tracers, J. Atmos. Chem., 39, 303–325, 2001.